Processive translocation mechanism of the human Bloom's syndrome helicase along single-stranded DNA

Máté Gyimesi[1], Kata Sarlós[1] and Mihály Kovács[1,*]

[1]Department of Biochemistry, Eötvös University, Pázmány P. s. 1/c, H-1117 Budapest, Hungary

ABSTRACT

BLM, one of the human RecQ helicases, plays a fundamental role in homologous recombination-based error-free DNA repair pathways, which require its translocation and DNA unwinding activities. Although translocation is essential *in vivo* during DNA repair processes and it provides a framework for more complex activities of helicases, including strand separation and nucleoprotein displacement, its mechanism has not been resolved for any human DNA helicase. Here, we present a quantitative model for the translocation of a monomeric form of BLM along ssDNA. We show that BLM performs translocation at a low adenosine triphosphate (ATP) coupling ratio (1 ATP consumed/1 nucleotide traveled) and moderate processivity (with a mean number of 50 nucleotides traveled in a single run). We also show that the rate-limiting step of the translocation cycle is a transition between two ADP-bound enzyme states. Via opening of the helicase core, this structural change may drive the stepping of BLM along the DNA track by a directed inchworm mechanism. The data also support the conclusion that BLM performs double-stranded DNA unwinding by fully active duplex destabilization.

INTRODUCTION

DNA and RNA helicases are nucleotide triphosphate (NTP)-consuming motor enzymes generating single-stranded (ss) forms of nucleic acids during fundamental cellular processes including replication, recombination and genome repair. RecQ-family DNA helicases are members of helicase superfamily 2 (SF2) involved in homologous recombination (HR)-based error-free DNA repair of double-stranded (ds) DNA breaks (DSBs) (1–4). Loss of function of BLM, one of the human RecQ helicases, causes Bloom's syndrome, a severe autosomal genetic disease leading to high cancer predisposition (5,6). BLM was recently proposed to suppress or promote HR depending on cellular conditions (7). BLM exerts its anti-recombinogenic activity by preventing premature initiation of HR via dissociation of Rad51 nucleoprotein filaments. This anti-recombination role of BLM is reflected in the hyperrecombination phenotype of Bloom's syndrome cells (5,8). On the other hand, BLM has also been proposed to be a key player in the synthesis-dependent strand annealing (SDSA) pathway of HR-based DSB repair (9). BLM can dissolve double Holliday junctions (10,11) and D-loops (12,13), and also stimulates DNA synthesis on model replication forks resembling one end of the D-loop by unwinding the displaced strand (7). In these processes, BLM must be able to perform adenosine triphosphate (ATP)-driven translocase, DNA helicase and branch migration activities.

Despite the fact that the biological functions of RecQ helicases have been widely investigated (14), their mechanisms of action are poorly understood. ATP-dependent translocation along ssDNA is the basis for the separation of the strands of dsDNA. Mechanistic knowledge about translocation thus provides a framework for more complex activities of DNA helicases, including dsDNA unwinding, branch migration and dissolution of double Holliday junctions (15). Moreover, ssDNA translocation itself is likely essential *in vivo* in DNA repair. At the initial phase of HR-based DSB repair, the BLM-induced disruption of Rad51 nucleoprotein filaments requires ssDNA translocation activity of BLM (7). Similarly, the translocation activity of the yeast Srs2 helicase is necessary for the catalysis of Rad51 nucleoprotein filament disassembly (16). ssDNA translocation-based unwinding of model replication forks also stimulates DNA synthesis by η polymerase, which role was reported in DSB repair

(17), supporting a proposed key function of BLM in SDSA (9). SDSA also involves facilitated annealing of complementary ssDNA stretches that form after D-loop disruption (2,18). The capability of translocation along ssDNA is likely essential *in vivo* for efficient strand annealing.

In biochemical and genetic studies and crystal structures of UvrD, there remains a controversy whether the monomeric form of this enzyme is capable of unwinding dsDNA (19–23). Studies on PcrA and Rep demonstrated that these SF1 helicases are able to perform translocation but are unable to unwind dsDNA substrates in their monomeric forms (24,25). By contrast, N-terminal truncation of BLM abolishes oligomerization, while the monomeric enzyme form retains its ATPase and DNA unwinding activities (26,27). These findings suggest a different mode of coupling between translocation and strand separation activities of BLM from those of the bacterial SF1 helicases.

Translocation along ssDNA requires processive movement of the helicase: the motor must be able to perform multiple enzymatic cycles and coupled mechanical steps before dissociating from its track. To date, three different models have been proposed to explain the translocation mechanisms of SF1 and SF2 helicases: (i) The 'inchworm' stepping mechanism for the monomer form of PcrA (28) and UvrD (19); (ii) the 'Brownian motor' (thermal ratchet) for hepatitis C virus NS3 helicase (29); and (iii) a 'non-uniform stepping model' for UvrD (30) and RecBCD DNA helicases (31) and NS3 helicase (32). The inchworm and Brownian models assume the hydrolysis of a single ATP molecule per kinetic step, dictated by the rate-limiting step of the cycle, which also defines the DNA-activated steady-state ATPase activity. The inchworm mechanism supports unidirectional processive stepping, while a Brownian motor oscillates between weakly and tightly DNA-bound states with diffusion-driven movements occurring in the weakly bound states. Therefore, enzymes using the inchworm stepping mechanism perform processive translocation at a low ATP coupling ratio [≤1 ATP hydrolyzed/nucleotide (nt) traveled], while those using the Brownian ratchet model generally translocate at a higher ATP coupling ratio.

In this study, we determined all key parameters of the ATP-driven translocation of BLM along ssDNA, using signals directly monitoring ATP consumption as well as the interaction of the enzyme with ATP and DNA at high temporal resolution (Figure 1, Table 1). We demonstrate that the monomeric form of BLM is a moderately processive DNA translocase (on average, performing 50 ATPase cycles during a processive run) with a low ATP coupling ratio (1 ATP consumed/1 nt traveled). During translocation, neither the ATP hydrolysis step nor any product release steps are rate limiting in the kinetic cycle. We propose that BLM translocates along ssDNA using an active, probably inchworm-like mechanism in which the rate-limiting step is a structural transition between two ADP-bound states, which may directly lead to stepping along ssDNA. Our results also show that the rate of ssDNA translocation matches that of dsDNA
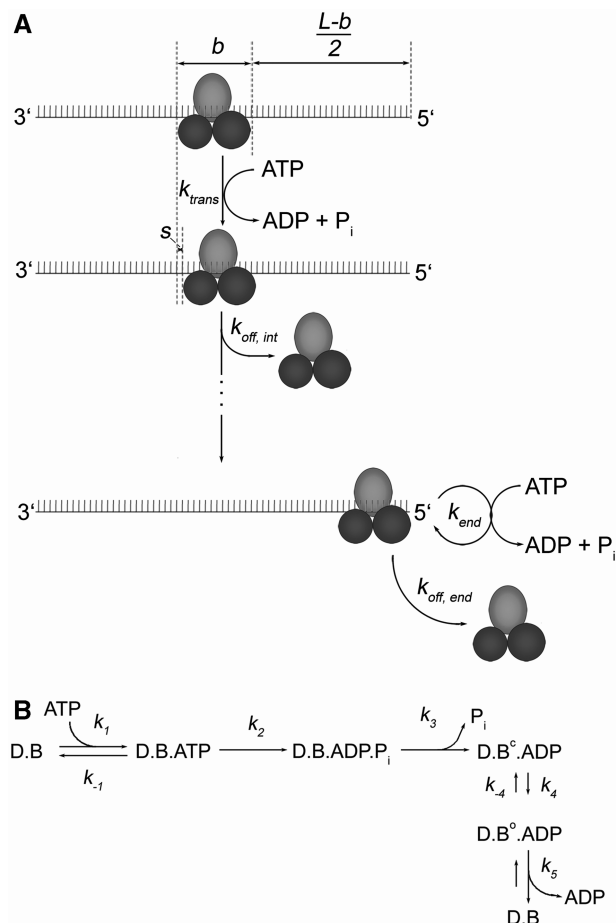

Figure 1. Model for BLM^{HM} translocation along ssDNA. **(A)** Scheme illustrating key translocation parameters. (Line 1) BLM^{HM} (RecA folds and C-terminal regions shown in dark and light gray, respectively) binds to ssDNA (L nucleotides in length) at a random location, occupying an ssDNA stretch of b nucleotides (binding site size). (Line 2) One DNA-bound ATP hydrolysis cycle (occurring at rate constant k_{trans}) displaces BLM^{HM} by s nucleotides (step size) toward the 5'-end. The mean number of cycles BLM^{HM} must undergo before reaching the terminus is thus $(L-b)/2s$. (Line 3) BLM^{HM} bound to ssDNA at the 5'-end has an ATPase turnover rate constant k_{end}. BLM^{HM} dissociates from internal sites of ssDNA and from the 5'-end at rate constants $k_{off, int}$ and $k_{off, end}$, respectively. **(B)** Dissection of the ATPase cycle of ssDNA-bound BLM^{HM} ($D.B$) during translocation (occurring at a net cycling rate k_{trans}). ATP binding (k_1) is followed by ATP hydrolysis (k_2) and P_i release (k_3). A structural transition between a closed (B^C) and an open (B^O) ADP-bound BLM^{HM} state (k_4) precedes ADP release (k_5). Table 1 shows parameters determined in this study.

unwinding (27), which supports a model in which BLM actively destabilizes the DNA duplex to perform rapid and efficient strand separation.

MATERIALS AND METHODS

Cloning and purification of BLM^{HM} as well as preparation of materials are described in Supplementary Data. All measurements were done at 25°C. DNA concentrations are expressed as those of oligo- or polynucleotide molecules (as opposed to those of constituent nucleotides).

Table 1. Kinetic parameters of BLM^{HM} translocation along ssDNA

	Method of determination	Value
ATP hydrolysis cycle		
k_1 ($\mu M^{-1} s^{-1}$)	mdATP	6.9 ± 0.7
k_{-1} ($-^{-1}$)	mdATP	120 ± 10
k_2 (s^{-1})	MDCC-PBP	>100
k_3 (s^{-1})	MDCC-PBP	>100
k_4 (s^{-1})	mdADP chasing	5.3 ± 0.6
k_{-4} (s^{-1})	mdADP chasing	≈ 2
k_5 (s^{-1})	mdADP chasing	270 ± 30
	mdADP binding	110 ± 30
k_{-5} ($\mu M^{-1} s^{-1}$)	mdADP binding	10 ± 1
ssDNA translocation		
k_{trans} (steady-state ATP hydrolysis rate constant during translocation, s^{-1})	PK/LDH assay, modeling	33 ± 2
	MDCC-PBP	27 ± 2
k_{end} (steady-state ATP hydrolysis rate constant at 5′-end, s^{-1})	PK/LDH assay, modeling	5.6 ± 0.5
$k_{off, int}$ (dissociation from ssDNA during translocation, s^{-1})	Trp fluorescence	≈ 0.2
$k_{off, end}$ (dissociation from 5′-end, s^{-1})	Trp fluorescence, PK/LDH assay, modeling	2.7 ± 0.3
P (processivity: probability of taking the next translocation step)[a]	Calculated	0.98
b (binding site size in nucleotides)	HEX fluorescence, mdADP, PK/LDH assay	14
	MDCC-PBP	12.4 ± 0.1
s (translocation step size in nucleotides)	MDCC-PBP	1.1 ± 0.1
ATP coupling ratio (ATP consumed/nucleotide traveled)	MDCC-PBP	0.87 ± 0.08

[a]The mean number of translocation steps taken in a single run is $P/(1 - P) = 50$.
Nomenclature refers to Figure 1. Means $\pm$ SEM values are shown for $n = 3$.

Fluorescence emission spectra were recorded in a SPEX FluoroMax spectrofluorometer in SF-50 buffer (50 mM Tris–HCl pH 7.5, 50 mM NaCl, 1 mM DTT, 5 mM MgCl$_2$) plus 10% glycerol. Fluorescein (FLU) and hexachlorofluorescein (HEX) emission was detected at 500–550 and 542–580 nm, with 494-nm and 538-nm excitation, respectively.

Transient kinetic measurements were carried out in a KinTek SF-2004 stopped-flow apparatus. Post-mix concentrations are stated in the text. P$_i$ release measurements were performed in SF-150 buffer (SF-50 buffer plus NaCl to 150 mM). A P$_i$ mop (150 μM 7-methylguanosine, 0.1 U/ml purine nucleoside phosphorylase) was present in all solutions. MDCC-PBP fluorescence was excited at 436 nm, and emission was followed through a 455-nm cutoff filter. Single-round translocation experiments were performed in the presence of heparin (see also Supplementary Data) in SF-50 buffer. 3′-(N-methyl-anthraniloyl)-2′-deoxy-ATP (mdATP) binding and release were measured in SF-50 buffer and mant fluorescence was detected through a 400-nm cutoff filter using 280-nm excitation, utilizing Förster resonance energy transfer (FRET) from BLM^{HM}'s aromatic residues. Trp fluorescence was excited at 297 nM, and emission was detected through a 340-nm interference filter.

Steady-state ATPase activities of BLM^{HM} (35 nM) were measured using a pyruvate kinase/lactate dehydrogenase (PK/LDH) coupled assay (14 U/ml PK, 20 U/ml LDH, 1 mM ATP, 1 mM phosphoenol pyruvate, 200 μM NADH) in SF-50 buffer plus 50 μg/ml BSA. Time courses of NADH absorbance ($\varepsilon_{340\,nm} = 6220\,M^{-1}\,cm^{-1}$) were followed in a Shimadzu UV-2101PC spectrophotometer. Oligonucleotide sequences are shown in Supplementary Data.

Data analysis, fitting and simulations were performed using OriginLab 7.5, KinTek SF-2004, and Gepasi v3.30 (www.gepasi.org). If not otherwise stated, reported uncertainties are standard errors of NLLS fits.

RESULTS

BLM^{HM} binds to ssDNA at random locations

In this study, we used BLM^{HM} (amino acids 642–1290), a fully active monomeric form of BLM that retains all activities and substrate specificities of the full-length enzyme (26). Fluorescence titration of 54-mer ssDNA molecules labeled either at the 3′-end or at the 5′-end with BLM^{HM} showed very similar hyperbolic binding profiles and apparent dissociation constants (Supplementary Figure S1A), demonstrating that nucleotide-free BLM^{HM} binds randomly and non-cooperatively along ssDNA with no end preference. To further assess DNA-binding properties, BLM^{HM} was mixed with equimolar amounts or 4-fold excess of 5′-labeled oligo-dT substrates of different lengths. The dependence of fluorescence change amplitudes on oligo-dT length corroborated random binding (Supplementary Figure S1B).

ATP binding to BLM^{HM} is uncoupled to ssDNA binding

ATP binding to BLM^{HM} was directly monitored in stopped-flow experiments using mdATP, a fluorescent ATP analogue (Supplementary Figure S1C). The mdATP concentration dependence of the observed rate constants (k_{obs}) of single-exponential binding transients indicated that ATP binding (step 1 in Figure 1B) is an apparently single-step, rapid and reversible process (Table 1). mdATP binding transients were practically uninfluenced by the presence of ssDNA, showing that ssDNA and ATP

binding to BLM^{HM} are uncoupled, similarly to that observed recently with forked dsDNA substrate (27) and that for DbpA RNA helicase (33).

ATP hydrolysis is rapid and favorable only in the DNA-bound form of BLM^{HM}

The kinetics of release of P_i produced during ATP hydrolysis were followed using MDCC-PBP, a fluorescently-labeled P_i binding protein (34). When BLM^{HM} plus dT_{54} was mixed with different concentrations of ATP in the stopped-flow, MDCC-PBP fluorescence transients consisted of an exponential burst followed by a linear steady-state phase (Figure 2A). The k_{obs} of the exponential burst ($67 \pm 6 \, s^{-1}$, SD for $n = 7$) was independent of ATP concentration. This rate constant was limited by P_i binding to MDCC-PBP, in concert with earlier reports (34) and our MDCC-PBP P_i binding calibration transients (Supplementary Data, Supplementary Figure S2). The amplitude of the burst showed hyperbolic dependence on ATP concentration (Figure 2B). The released P_i/BLM^{HM} molar ratio saturated at around unity, which indicates that the ATP hydrolysis and P_i release steps (k_2 and k_3 in Figure 1B, Table 1) are practically irreversible, and the rate-limiting step of the enzymatic cycle during translocation occurs after P_i release. Steady-state k_{cat} (maximal steady-state turnover rate constant) and K_{ATP} (half-saturating ATP concentration) values were

determined from slopes of the linear phase of MDCC-PBP fluorescence transients (Figure 2B inset). K_{ATP} ($20 \, \mu M$) was close to the ATP binding K_d ($17 \, \mu M$) calculated from mdATP binding kinetics (Figure 2B inset, Supplementary Figure S1C, Table 1), indicating that K_{ATP} is dictated by reversible ATP binding.

In another set of experiments, BLM^{HM} was preincubated with different concentrations of dT_{54} and then rapidly mixed with ATP (at saturating concentration) in the stopped flow. In the absence of dT_{54}, a low-amplitude P_i burst ($A_{burst} = 0.05 \, mol \, P_i/mol \, BLM^{HM}$) was observed with a k_{obs} similar to those in the presence of dT_{54} (Figure 2C). This behavior implies that in DNA-free BLM^{HM}, ATP hydrolysis and P_i release occur rapidly but ATP hydrolysis is unfavorable with an apparent equilibrium constant of 0.05 ($= A_{burst}/(1 - A_{burst})$). ($P_i$ release is quasi-irreversible in the presence of MDCC-PBP.) Traces in the absence and presence of dT_{54} at different concentrations consisted of exponential burst and linear steady-state phases (Figure 2C). The k_{obs} of the exponential burst was independent of dT_{54} concentration and was identical to that in the experiments of Figure 2A. The released P_i/BLM^{HM} molar ratio calculated from the P_i burst amplitudes saturated at around unity (Figure 2D), again corresponding to rapid pre-steady-state ATP hydrolysis before the steady-state phase. The steady-state ATPase activity of BLM^{HM}, calculated from
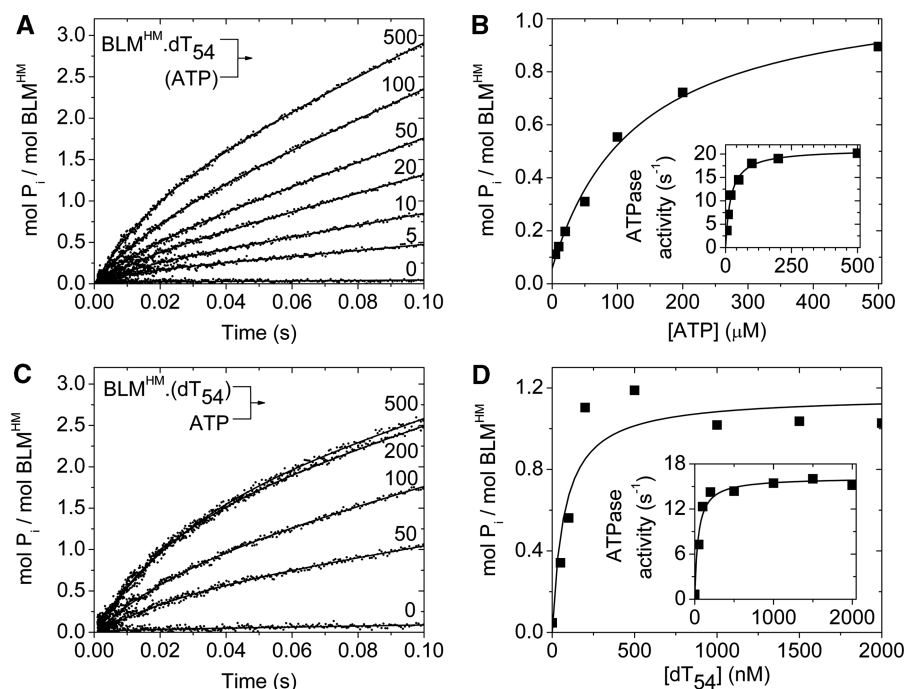

Figure 2. Dependence of transient P_i production on ATP and ssDNA concentration. (**A**) Kinetics of P_i production from ATP upon mixing $0.25 \, \mu M$ BLM^{HM} plus $2 \, \mu M \, dT_{54}$ with ATP (concentrations in μM indicated) in the stopped-flow, as monitored by MDCC-PBP fluorescence ($2 \, \mu M$ in all syringes). Traces were fitted with exponential plus linear functions. Conversion of MDCC-PBP fluorescence to mol P_i/mol BLM^{HM} ratio was based on the calibration curve shown in Supplementary Figure S2. In the absence of ATP, no change in MDCC-PBP fluorescence was detected. (**B**) Dependence of the amplitudes of the rapid exponential burst (main panel; maximal burst = $1.1 \pm 0.1 \, mol \, P_i/mol \, BLM^{HM}$) and steady-state ATP consumption rates (inset; calculated from the slope of the linear phase) on ATP concentration ($k_{cat} = 21 \, s^{-1}$, $K_{ATP} = 20 \, \mu M$). (**C**) Kinetics of P_i production upon mixing $0.25 \, \mu M \, BLM^{HM}$ plus dT_{54} (concentrations in nM indicated) with $500 \, \mu M$ ATP. (**D**) Dependence of the amplitudes of the exponential burst (main panel; maximal burst = $1.2 \pm 0.2 \, mol \, P_i/mol \, BLM^{HM}$) and steady-state ATP consumption rates (inset) on dT_{54} concentration ($k_{cat} = 16 \, s^{-1}$, $K_{DNA} = 44 \, nM$).

the slope of the linear phase, was markedly activated by dT_{54} (Figure 2D inset, cf. Figure 2B inset).

The ssDNA length-dependence of the P_i release profile was determined by preincubating $0.25\,\mu M$ BLM^{HM} with $2\,\mu M$ oligo-dT substrates of different length (dT_{18}, dT_{36} and dT_{54}), followed by rapid mixing with $500\,\mu M$ ATP in the stopped flow. The amplitude of the rapid exponential burst of the MDCC-PBP fluorescence transients was practically identical in dT_{18}, dT_{36} and dT_{54} (the released P_i/BLM molar ratio was 1.2 ± 0.5, SD for $n = 3$), again indicating pre-steady-state ATP hydrolysis (cf. Figure 2B and D).

ADP release experiments identify the rate-limiting step and indicate that BLM^{HM} occupies a ssDNA stretch of 14 nt

We followed the transient kinetics of mdADP release from BLM^{HM} in 'chasing' experiments in which we rapidly mixed a premixture of BLM^{HM}, mdADP and varying concentrations of oligo-dT substrates of different length (dT_{18}, dT_{36} and dT_{54}) with excess unlabeled ATP in the stopped flow. In the absence of DNA, the dissociation of mdADP from BLM^{HM} resulted in a biphasic fluorescence decrease with k_{obs} values of $29\,s^{-1}$ and $0.38\,s^{-1}$, with the rapid phase having a fractional amplitude of 72% (Figure 3A). This result indicates that the BLM^{HM}.ADP complex adopts two states in solution: the rapid phase corresponds to an 'open' state from which ADP can freely dissociate, whereas the slow phase indicates a 'closed' subpopulation that must first slowly convert to the open state to release ADP (step 4 in Figure 1B). This conclusion is in line with previous implications that the stimulatory effect of DNA on the BLM^{HM} ATPase activity is brought about by an enhancement of the rate of the ADP dissociation process (27). Importantly, however, here we directly show that it is not the ADP dissociation step itself but a conformation change preceding ADP release that is rate limiting during the translocation cycle. In line with this, mdADP binding to apo-BLM^{HM} resulted in biphasic transients; the presence

of the slow phase (with a $k_{obs} \sim 0.4\,s^{-1}$) confirmed the slow isomerization reaction from the closed to open state of BLM^{HM} (Supplementary Figure S3). In the presence of increasing concentrations of oligo-dT, the k_{obs} of the rapid and slow phases in the 'chasing' experiments increased to $270 \pm 30\,s^{-1}$ and $5.3 \pm 0.6\,s^{-1}$, respectively (Figure 3A). In the presence of DNA, mdADP binding was also biphasic with a slow phase k_{obs} of $8.1 \pm 0.3\,s^{-1}$ [corresponding to $(k_4 + k_{-4})$ in Figure 1B], which again corroborates that the closed-open transition (represented in the slow phase) is the rate-limiting step during the steady-state translocation cycle (Figure 1B, Table 1). The rate constants of the isomerization phase were somewhat lower than the maximal DNA-activated ATPase activity of BLM^{HM} in P_i release experiments (Figure 2D inset). This difference can possibly result from the presence of the fluorescent label in mdADP. [Besides several studies on cytoskeletal motor proteins (35–37), it was recently reported that mantADP binds with a >40-fold higher affinity to PcrA than unlabeled ADP (38).]

The presence of ssDNA had a marked effect on the magnitude of total fluorescence changes upon mdADP release. The dependence of this parameter on oligo-dT concentration turned out to be a highly useful indicator of the stoichiometry of BLM^{HM} binding to oligo-dT substrates of different length (Figure 3B). In contrast to recent results (27), the BLM^{HM}.ADP complex exhibited high-affinity oligo-dT binding profiles, from which we deduced BLM^{HM}/oligo-dT molar ratios of 0.95 ± 0.17, 2.0 ± 0.2, and 3.8 ± 0.6 for dT_{18}, dT_{36} and dT_{54}, respectively (Figure 3B). The result for dT_{54}, which is the least affected by DNA end-effects, indicates that a single BLM^{HM} molecule occupies an ssDNA stretch of about 14 nt (parameter b in Figure 1A, Table 1). This binding site size was confirmed in other experiments (see below).

In the experiments of Figure 3, the k_{obs} of mdADP fluorescence transients and the fractional amplitudes of the two phases were independent of mdADP concentration (10–$100\,\mu M$) in all cases. [The rapid phase had a fractional
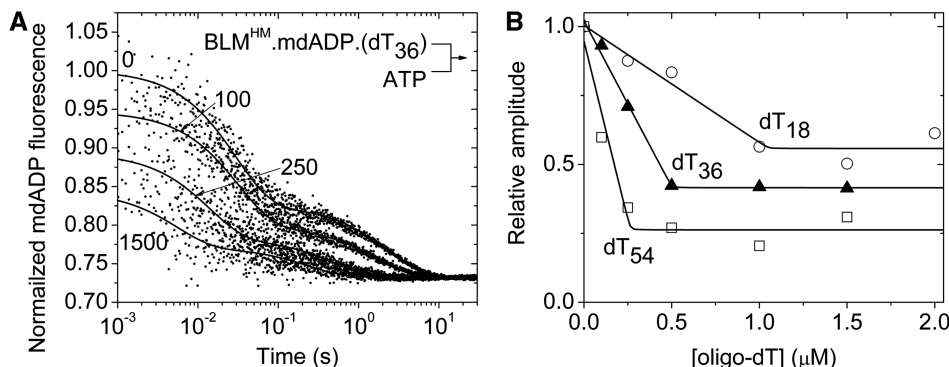

Figure 3. Kinetics of mdADP release and stoichiometry of BLM^{HM} binding to ssDNA. (**A**) mdADP fluorescence transients recorded upon mixing a premixture of $1\,\mu M$ BLM^{HM}, $20\,\mu M$ mdADP plus dT_{36} (concentrations in nM indicated) with $2.5\,mM$ ATP in the stopped flow. Double exponential fits to the data are shown. Fitted parameters are discussed in the text. (**B**) Dependence of relative amplitudes of mdADP fluorescence transients (A) on the concentration of oligo-dT substrates of different length. (Total amplitudes in the absence of oligo-dT were taken as unity.) Solid lines indicate fits based on a quadratic equation for the binding of BLM^{HM} to oligo-dT described in Supplementary Data. Binding stoichiometries obtained from the fits are discussed in the text. Fits produced DNA binding K_d values <$0.1\,\mu M$.

amplitude of $79 \pm 4\%$ (SD for $n = 10$) at $10\,\mu M$ mdADP and $71 \pm 5\%$ at $100\,\mu M$ mdADP.] These results, together with those of Supplementary Figure S3, indicate that the experiments of Figure 3A truly report on the process of multistep mdADP dissociation instead of phenomena related to multiple binding sites or binding modes.

BLM^{HM} consumes one ATP per nucleotide traveled

Heparin has been used as a protein trap to generate single-round conditions in which the helicase cannot rebind to the DNA track after dissociation (20,30,39). Heparin has no ATPase activity, and accelerates DNA-free BLM^{HM} ATPase activity only 2.5-fold (Supplementary Figure S4). When BLM^{HM} was preincubated with saturating concentrations of oligo-dT substrates of different length and then rapidly mixed in the stopped-flow with ATP plus heparin, the MDCC-PBP fluorescence transients showed a multiphasic P_i release profile (Figure 4A). Traces with substrates longer than the binding site size consisted of a rapid exponential burst and two distinct linear phases, while in those with dT_{12} the first, more rapid linear phase was lacking (Figure 4A, inset). The amplitude of the exponential burst was practically equivalent to the pre-steady-state

hydrolysis of one ATP per enzyme molecule ($A_{burst} = 1.1 \pm 0.1\,\text{mol } P_i/\text{mol BLM}^{HM}$) as previously seen in the absence of heparin (Figure 2), and its k_{obs} ($55 \pm 12\,\text{s}^{-1}$, SD for $n = 12$) was also similar to those obtained in the absence of heparin. This exponential phase therefore represents the first round of ATP hydrolysis by DNA-bound BLM^{HM}. The ATP turnover rates calculated from the first linear phase were independent of oligo-dT length above $12\,\text{nt}$ ($27 \pm 2\,\text{s}^{-1}$, SD for $n = 12$). The amplitudes of this phase increased with oligo-dT length (Figure 4B), indicating that they represent ATP consumption during translocation of BLM^{HM} along ssDNA. Based on our recently published analytical method (40), the amplitude data revealed that the presence of heparin decreased the processivity of BLM^{HM} (Figure 4B; see also Supplementary Data). The processivity at zero heparin concentration was $P = 0.98$ (expressed as the probability of a translocation step), corresponding to a mean run length ($P/(1 - P)$) of 50 steps (Figure 4C, see also Supplementary Data) (40). The step size ($s = 1.1 \pm 0.1\,\text{nt}$ traveled per ATP hydrolyzed, corresponding to an ATP coupling ratio of 0.87 ATP/nt) and binding site size ($b = 12.4 \pm 0.1\,\text{nt}$) were independent of heparin concentration (Figures 4B and 1A, Table 1). The
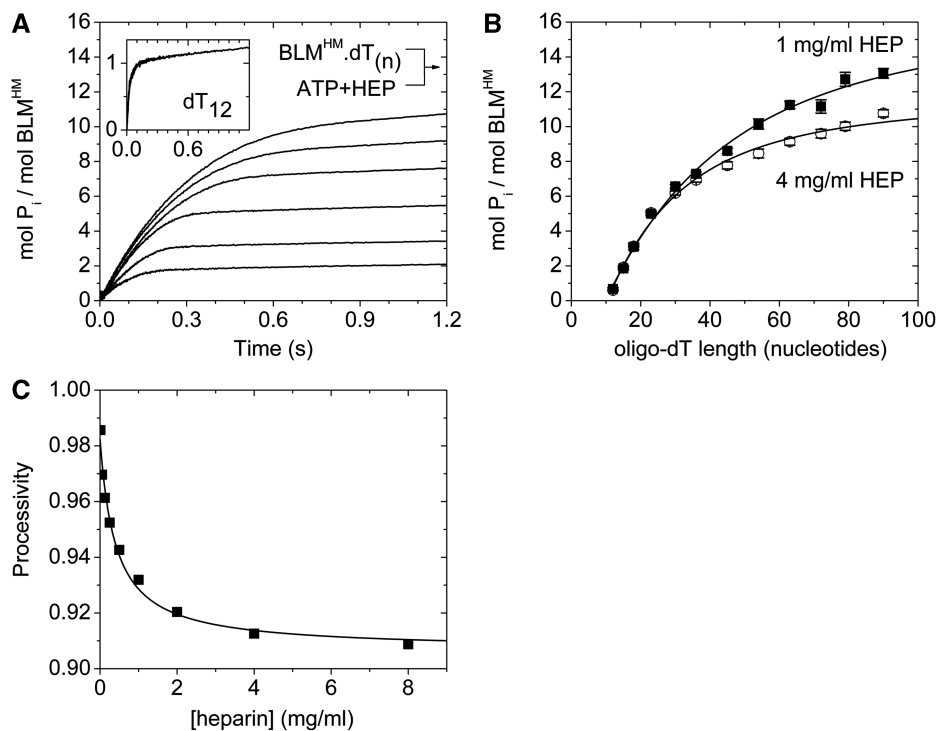

Figure 4. Single-round translocation experiments. (**A**) Transient kinetics of P_i production from ATP upon mixing $0.1\,\mu M$ BLM^{HM} plus $2.5\,\mu M$ oligo-dT with $500\,\mu M$ ATP plus $1\,\text{mg/ml}$ heparin in the stopped flow, as monitored by MDCC-PBP fluorescence ($2\,\mu M$ in all syringes). Traces consisted of an exponential burst and two distinct linear phases. Oligo-dT lengths were (bottom to top) 15, 18, 23, 36, 45 and 54 nt. The inset shows the reaction with dT_{12}. Conversion of MDCC-PBP fluorescence to mol P_i/mol BLM^{HM} ratio was based on a calibration curve (Supplementary Figure S2). (**B**) Oligo-dT length-dependence of P_i production (mol P_i/mol BLM^{HM}) occurring before the end of the first linear phase (corresponding to BLM^{HM} translocation along oligo-dT). The fit to the data indicated a coupling ratio of 0.87 ± 0.08 ATP/nucleotide traveled (independent of heparin concentration). Note that P_i production values include P_i produced during the initial exponential burst, and data points only above the binding site size were used in the fit. Binding site size was also left to float and resulted very similar values ($b = 12.4 \pm 0.13\,\text{nt}$) to those determined in other experiments (Figures 3B and 5B). (**C**) Dependence of the determined processivities of BLM^{HM} translocation along oligo-dT on heparin concentration. The processivity extrapolated to zero heparin concentration was 0.98. Equations for NLLS fits used in (B) and (C) are described in Supplementary Data and in Ref. 40.

binding site size was very similar to that determined in the experiments of Figure 3B. The ATP consumption rate during the second linear phase ($0.14 \pm 0.08\,s^{-1}$, SD for $n = 12$) was similar to the steady-state ATPase rate of heparin-bound BLM^{HM} (Supplementary Figure S4), indicating that this phase mainly corresponds to steady-state ATP hydrolysis by heparin-bound BLM^{HM} after it has dissociated from DNA. In line with this, this value also matches the ATPase rate in the linear phase in experiments with dT_{12} where the lack of a more rapid linear phase indicated the lack of translocation due to the short length of DNA (Figure 4A).

To corroborate the translocation parameters described above, we also performed experiments monitoring P_i release during single-round translocation of BLM^{HM} on m13 circular ssDNA (Supplementary Figure S5), as well as Trp fluorescence experiments monitoring the dissociation of BLM^{HM} from ssDNA (Supplementary Figure S6).

Dependence of steady-state ATP consumption on ssDNA length corroborates the kinetic model of translocation

The steady-state ATPase activity of DNA-free BLM^{HM}, determined using a PK/LDH coupled assay ($k_{cat} = 0.081 \pm 0.007\,s^{-1}$, SD for $n = 8$, $K_{ATP} = 26 \pm 3\,\mu M$), was strongly activated by non-repetitive sequence oligonucleotides ($k_{cat, DNA\_54mer} = 13\,s^{-1}$), oligo-dT ($dT_5 - dT_{90}$) (Figures 2 and 5) and m13mp18 circular ssDNA ($k_{cat, m13} = 13\,s^{-1}$). From these data, it is obvious that oligo-dT activated the ATPase activity slightly more (within a factor of two) than non-repetitive sequence oligonucleotides of the same length and m13 phage ssDNA. Moreover, oligo-dT_{90} substrate with phosphorothioate (PTO) modification also stimulated the ATPase activity of BLM^{HM} with

similar degree as the unmodified dT_{90} ($k_{cat, PTO-dT90} = 20\,s^{-1}$) (Figure 5).

We titrated BLM^{HM} with increasing oligo-dT concentrations to determine the DNA concentration necessary for half-maximal ATPase activation (K_{DNA}) at saturating ATP concentration. K_{DNA} steeply decreased with increasing oligo-dT length until the length exceeded the binding site size ($b = 14\,nt$) (Figure 5A (inset); cf. Figures 3B and 4B). At longer lengths, the shallow decrease in K_{DNA} was mostly dictated by the binding stoichiometry of BLM^{HM} to oligo-dT substrates of different length (cf. Figure 3B). This was even more apparent when the K_{DNA} data were converted into the molar excess of DNA binding sites over BLM^{HM} (Figure 5A).

Importantly, the maximal ssDNA-activated ATPase turnover rates (k_{cat}) showed a characteristic length-dependent profile (Figure 5B). The k_{cat} values using longer oligo-dT substrates are in good agreement with those measured recently with full-length BLM (7) indicating that the monomeric form of BLM utilizes the same translocation mechanism as the full-length form. k_{cat} stagnated in the length range of 7–12 nt ($\sim5\,s^{-1}$, corresponding to k_{end} in Figure 1A, Table 1), then steeply increased to a maximal value of $\sim25\,s^{-1}$ (confirming that the first linear phase in Figure 4A corresponds to the ATP consumption rate during translocation along ssDNA), already reaching quasi-saturation at a length of $\sim60\,nt$. This profile matches the predictions expected from the kinetic model of BLM^{HM} translocation based on the presented experiments (Figure 5B legend, Table 1, 'Discussion' section and Supplementary Data).

The K_{DNA} values of Figure 5A also support that, in kinetic experiments performed at a single DNA concentration (Figures 2A and B, 4, 5B, S1C, S3 and S5 and 6), the applied DNA concentration (typically micromolar) was quasi-saturating and high enough to rule out the possibility that the results were influenced by
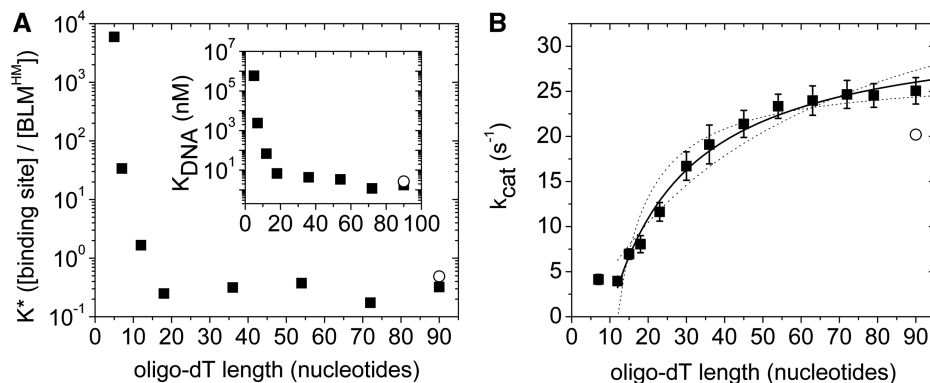

Figure 5. ssDNA length-dependence of steady-state parameters. (**A**) Molar excess of DNA binding sites over BLM^{HM} required for half-maximal ATPase activation (K^*) at different oligo-dT lengths. K^* values were calculated using $b = 14\,nt$ and DNA concentrations required for half-maximal ATPase activation (K_{DNA} at 35 nM BLM^{HM}, inset). (**B**) Dependence of the maximal DNA-activated ATPase activity (k_{cat}) on oligo-dT length [(ATP) = 1 mM]. Oligo-dT concentrations used to determine k_{cat} at different lengths were 40 µM for dT_7, 1 µM for dT_{12-18}, 0.5 µM for dT_{23}, 100 nM for dT_{30-90} and PTO-modified dT_{90}. Open circles show the K_{DNA} and k_{cat} values obtained with PTO-modified dT_{90} substrate in (A) and (B), respectively. Uncertainties are standard deviations of replicate trials with three different BLM^{HM} preparations. The solid line in (B) is a fit based on the model shown in Figure 1A. (Fits using the equation described in Supplementary Data produced very similar results to global kinetic simulations based on the determined kinetic parameters.) The best fit (solid line) was obtained at values shown in Table 1. The robustness of the fit is indicated by the dotted lines representing simulations at $k_{off, end}$ values twice as high/low as the best fit.

simultaneous binding of multiple BLM^{HM} molecules to the same DNA molecule.

DISCUSSION

Dissection of the BLM^{HM} ATP hydrolysis cycle leading to ssDNA translocation

During an enzymatic cycle leading to translocation along ssDNA (occurring at a net turnover rate k_{trans} in Figure 1A), ATP binding is followed by hydrolysis and product release steps (Figure 1B, Table 1). Our results reveal the following salient features of this cycle: (i) ATP binding is rapid, reversible, and unaffected by ssDNA (Figure 2 and Supplementary Figure S1C). (ii) In ssDNA-bound BLM^{HM}, ATP hydrolysis and P_i release are rapid, quasi-irreversible, and precede the rate-limiting step (Figures 2 and 4A). (iii) The rate-limiting step (probably a conformational transition) occurs between two ADP-bound BLM^{HM} states (Figure 3A). This step is markedly accelerated by ssDNA (Figure 3A).

Key parameters and distinctive features of the BLM^{HM} translocation mechanism

Processive translocation along DNA requires multiple ATP hydrolysis-coupled DNA-bound translocation steps. Figure 1A and Table 1 summarize the proposed translocation mechanism of BLM^{HM}, exhibiting the following key features: (i) DNA binding occurs randomly along ssDNA (Supplementary Figure S1A and B). (ii) The binding site size (b) is about 14 nt (Figures 3B, 4A and B and 5). (This is not necessarily equivalent to the contact site size of the BLM^{HM}–ssDNA complex; it is defined as the number of occluded nucleotides by a BLM^{HM} molecule.) This binding site size is somewhat larger than that reported recently (27). However, contrary to the results presented here, in that study the binding site size was determined only from the fit to anisotropy titration data, without confirmatory independent results. (iii) During one ATP hydrolysis cycle (occurring at a net rate k_{trans}), BLM^{HM} travels 1 nt along ssDNA (s) (Figure 4A and B). (iv) On reaching the 5′-end (where the ATPase cycle slows down to k_{end}), BLM^{HM} rapidly dissociates from ssDNA ($k_{off, end}$) (Figure 5B). (v) The rate constant of BLM^{HM} dissociation from ssDNA during translocation ($k_{off, int}$) is relatively low, resulting in a moderate translocation processivity (with a mean of 50 nt traveled in a single run) (Figure 4C, Table 1).

BLM can unwind dsDNA regions shorter than 100 nt in the absence of binding partners (6). BLM^{HM} was recently shown to unwind forked DNA substrates with low processivity (27), indicating that its unwinding processivity is somewhat lower than the translocation processivity determined in this study. However, the difference may at least partially result from the fact that the dependence of unwinding processivity on trap concentration was not determined (27). Interestingly, the unwinding step size of *Escherichia coli* RecQ helicase was 4 nt (41), a value that greatly differs from the unwinding step size of BLM^{HM} (27) and the translocation step size reported here.

However, a direct measurement of ATP consumption during unwinding is still lacking. The available data highlight the necessity of precise measurements of enzymatic parameters during dsDNA unwinding.

The kinetic mechanism of BLM translocation along ssDNA described here, the first one for a human helicase, displays several features that are different from those of other helicases. The key difference between the previously described translocation mechanisms of PcrA and UvrD (SF1) (30,42), RecG and Isw2 (SF2) (43,44) and that of BLM is that BLM performs DNA length-independent rapid pre-steady-state ATP hydrolysis before steady-state translocation (Figures 2 and 4A). This behavior is due to rapid, non-rate-limiting ATP binding, hydrolysis and P_i release (Table 1). In SF1 helicases, steady-state translocation was not preceded by a pre-steady-state burst in P_i production, indicating that the rate-limiting step precedes P_i release (30,42).

Another key property of the BLM mechanism is the low ATP coupling ratio (Figure 4B, Table 1). In line with PcrA and UvrD in which the hydrolysis of one ATP was observed per one translocated nucleotide on ssDNA (based on both solution measurements and on crystal structures), BLM also travels 1 nt per ATP hydrolysis. Although RecG was recently shown to exhibit a low ATP coupling ratio (1 ATP/3 nt), this indirect measurement was based on translocation rate during unwinding (44), which might significantly differ from that during ssDNA translocation.

A third important feature is that, after completing translocation, BLM does not perform multiple rounds of 'futile' ATP hydrolysis at the 5′ end. The characteristic ssDNA length-dependence of the ATPase activity (Figure 5B) indicates that BLM relatively rapidly dissociates from the 5′-end (at $k_{off, end}$) where its ATPase cycling rate (k_{end}) is lower than that during translocation (k_{trans}) (Figure 1A, Table 1). Although PcrA had been proposed to remain bound at the 5′-end and perform several slow enzymatic cycles before dissociation (very slow $k_{off, end}$), which resulting in a ssDNA length-independent steady-state ATPase activity governed by k_{end} (42), using longer DNA substrates PcrA also showed DNA length dependence of steady-state k_{cat} (38), indicating a mechanism similar to the one proposed in the current study. On the other hand, the ssDNA length-independent ATPase activity of UvrD (22) results from a different set of features, namely that the ATPase rates during translocation and at the ssDNA end are practically identical ($k_{trans} = 42\,s^{-1}$, $k_{end} = 40\,s^{-1}$) (20,30).

Implications of the proposed translocation model: enzyme–DNA interactions

The translocation mechanisms of PcrA, UvrD and Rep (SF1) have revealed an inchworm mechanism in which nucleotide bases of ssDNA form hydrophobic stacking interactions with aromatic residues of the enzyme, and nucleotide-induced conformational changes displace the ssDNA strand along the DNA-binding cavity (19,28,45). In contrast, recent studies on SF2 helicases (hepatitis C virus NS3, archaeal Hel308) support a translocation

mechanism based on protein-DNA backbone interactions (15,46,47). BLM contains the tryptophan (Trp[803]) that, based on its interaction with DNA nucleotide bases, has been identified as a key residue for the hydrophobic stacking-based mechanism and is conserved through SF1 and SF2 helicases (sequence alignments of the corresponding region of SF1 and SF2 helicases are shown in Supplementary Data, Table S1).

On the other hand, BLM also contains key structural elements proposed for a translocation mechanism based on enzyme-DNA backbone interactions. In existing atomic structures of DNA-bound viral NS3, *Drosophila* VASA and eIF4AIII (SF2) enzymes, two conserved threonines have been shown to play fundamental roles in helicase-DNA backbone interactions (47–51). One of these threonines is located in motif V, which is conserved among SF1 and SF2 enzymes. Structural and/or sequence similarities between motif V of NS3, Swi2/Snf2, RecQ and BLM suggest that this conserved threonine (Thr[946] in BLM) may play a similar role in BLM translocation as in NS3. The recently published atomic structure of DNA-bound RecQL1 (PDB code 2WWY) also reveals that this threonine (Thr[371] in RecQL1) is in direct contact with the backbone of the ssDNA strand spanning the surface of the RecA fold domains. The other conserved threonine is located in motif Ib of NS3, a region missing from RecQ helicases. Further structural similarities between NS3, Hel308, RecQ, and RecQL1 support the hypothesis that ssDNA binds to the large cleft formed by the two RecA fold domains and the RecQCt domain and that BLM residues may form contacts to the sugar-phosphate backbone of ssDNA.

Another possible mechanism for BLM translocation is a 'mixed mechanism', which was recently published for an SF1B helicase (52). In this case, both hydrophobic stacking and backbone interactions determine the translocation with 1 nt per one ATP hydrolysis (though in the 5′-3′ direction). This assumption is corroborated by the fact that in our experiments, PTO-modified oligo-dT_{90} activated BLM^{HM} to a similar degree as the unmodified oligo and K_{DNA} was also only slightly altered (Figure 5). This result indicates that BLM can translocate on DNA substrates with modified sugar phosphate backbone, but the translocation is somewhat slower.

Implications of the proposed translocation model: rate-limiting step and active dsDNA unwinding

The slow, rate-limiting conformational transition in ADP-bound BLM^{HM} identified in this work may represent the opening of the nucleotide-binding cleft formed by the two RecA-folds of the helicase module, which could result in a physical step along ssDNA. By contrast, a rate-limiting P_i release step was proposed to drive the power stroke used for unwinding by YxiN and NS3 RNA helicases (53,54).

It was recently proposed that DNA weakens the affinity of BLM^{HM} for ADP, thus accelerating the steady-state ATPase rate. Our present study points out that ADP release itself occurs rapidly, and the allosteric activation of the BLM^{HM} ATPase by DNA is brought about specifically via the acceleration of the slow structural transition preceding ADP release, presumably by the interaction of DNA with the large cleft spanning the whole length of the RecA domains. Crystal structures and homology modeling of SF1 and SF2 helicases (19,28,47,55,56) support that this structural change may enable ADP dissociation and stepping along the DNA track in an inchworm-like manner.

The present general framework for unwinding activities discriminates between two catalytic strategies: a 'passive' one in which the helicase moves forward and unwinds the substrate by exploiting the thermal fraying of DNA base pairs, in contrast to 'active' unwinding whereby the enzyme facilitates the destabilization of the duplex ahead of it (15,57–59). Based on this model, enzymes using a passive mechanism unwind double-stranded nucleic acid segments at significantly reduced rates compared to that of translocation along single-stranded nucleic acids. In contrast, optimally active enzymes can separate the two strands at the same rate as the translocation rate. Importantly, the ssDNA translocation rate of BLM^{HM} determined in this study is very similar to that reported for dsDNA unwinding by the same construct (27), which supports a fully active model for the dsDNA unwinding mechanism of BLM.

SUPPLEMENTARY DATA

Supplementary Data are available at NAR Online.

ACKNOWLEDGEMENTS

FUNDING

REFERENCES

1. Singleton,M.R., Dillingham,M.S. and Wigley,D.B. (2007) Structure and mechanism of helicases and nucleic acid translocases. *Annu. Rev. Biochem.*, **76**, 23–50.
2. Wu,L. and Hickson,I.D. (2006) DNA helicases required for homologous recombination and repair of damaged replication forks. *Annu. Rev. Genet.*, **40**, 279–306.
3. Bohr,V.A. (2008) Rising from the RecQ-age: the role of human RecQ helicases in genome maintenance. *Trends Biochem. Sci.*, **33**, 609–620.
4. Oh,S.D., Lao,J.P., Hwang,P.Y., Taylor,A.F., Smith,G.R. and Hunter,N. (2007) BLM ortholog, Sgs1, prevents aberrant crossing-over by suppressing formation of multichromatid joint molecules. *Cell*, **130**, 259–272.
5. German,J. (1993) Bloom syndrome: a mendelian prototype of somatic mutational disease. *Medicine (Baltimore)*, **72**, 393–406.

6. Karow,J.K., Chakraverty,R.K. and Hickson,I.D. (1997) The Bloom's syndrome gene product is a 3′-5′ DNA helicase. *J. Biol. Chem.*, **272**, 30611–30614.

7. Bugreev,D.V., Yu,X., Egelman,E.H. and Mazin,A.V. (2007) Novel pro- and anti-recombination activities of the Bloom's syndrome helicase. *Genes Dev.*, **21**, 3085–3094.

8. Langlois,R.G., Bigbee,W.L., Jensen,R.H. and German,J. (1989) Evidence for increased in vivo mutation and somatic recombination in Bloom's syndrome. *Proc. Natl Acad. Sci. USA*, **86**, 670–674.

9. Adams,M.D., McVey,M. and Sekelsky,J.J. (2003) Drosophila BLM in double-strand break repair by synthesis-dependent strand annealing. *Science*, **299**, 265–267.

10. Wu,L., Chan,K.L., Ralf,C., Bernstein,D.A., Garcia,P.L., Bohr,V.A., Vindigni,A., Janscak,P., Keck,J.L. and Hickson,I.D. (2005) The HRDC domain of BLM is required for the dissolution of double Holliday junctions. *EMBO J.*, **24**, 2679–2687.

11. Wu,L. and Hickson,I.D. (2003) The Bloom's syndrome helicase suppresses crossing over during homologous recombination. *Nature*, **426**, 870–874.

12. Bachrati,C.Z., Borts,R.H. and Hickson,I.D. (2006) Mobile D-loops are a preferred substrate for the Bloom's syndrome helicase. *Nucleic Acids Res.*, **34**, 2269–2279.

13. van Brabant,A.J., Ye,T., Sanz,M., German,I.J., Ellis,N.A. and Holloman,W.K. (2000) Binding and melting of D-loops by the Bloom syndrome helicase. *Biochemistry*, **39**, 14617–14625.

14. Bachrati,C.Z. and Hickson,I.D. (2008) RecQ helicases: guardian angels of the DNA replication fork. *Chromosoma*, **117**, 219–233.

15. Pyle,A.M. (2008) Translocation and unwinding mechanisms of RNA and DNA helicases. *Annu. Rev. Biophys.*, **37**, 317–336.

16. Antony,E., Tomko,E.J., Xiao,Q., Krejci,L., Lohman,T.M. and Ellenberger,T. (2009) Srs2 disassembles Rad51 filaments by a protein-protein interaction triggering ATP turnover and dissociation of Rad51 from DNA. *Mol. Cell*, **35**, 105–115.

17. McIlwraith,M.J., Vaisman,A., Liu,Y., Fanning,E., Woodgate,R. and West,S.C. (2005) Human DNA polymerase eta promotes DNA synthesis from strand invasion intermediates of homologous recombination. *Mol. Cell*, **20**, 783–792.

18. Ouyang,K.J., Woo,L.L. and Ellis,N.A. (2008) Homologous recombination and maintenance of genome integrity: cancer and aging through the prism of human RecQ helicases. *Mech. Ageing Dev.*, **129**, 425–440.

19. Lee,J.Y. and Yang,W. (2006) UvrD helicase unwinds DNA one base pair at a time by a two-part power stroke. *Cell*, **127**, 1349–1360.

20. Fischer,C.J., Maluf,N.K. and Lohman,T.M. (2004) Mechanism of ATP-dependent translocation of E. coli UvrD monomers along single-stranded DNA. *J. Mol. Biol.*, **344**, 1287–1309.

21. Maluf,N.K., Fischer,C.J. and Lohman,T.M. (2003) A dimer of Escherichia coli UvrD is the active form of the helicase in vitro. *J. Mol. Biol.*, **325**, 913–935.

22. Curti,E., Smerdon,S.J. and Davis,E.O. (2007) Characterization of the helicase activity and substrate specificity of Mycobacterium tuberculosis UvrD. *J. Bacteriol.*, **189**, 1542–1555.

23. Mechanic,L.E., Hall,M.C. and Matson,S.W. (1999) Escherichia coli DNA helicase II is active as a monomer. *J. Biol. Chem.*, **274**, 12488–12498.

24. Cheng,W., Hsieh,J., Brendza,K.M. and Lohman,T.M. (2001) E. coli Rep oligomers are required to initiate DNA unwinding in vitro. *J. Mol. Biol.*, **310**, 327–350.

25. Niedziela-Majka,A., Chesnik,M.A., Tomko,E.J. and Lohman,T.M. (2007) Bacillus stearothermophilus PcrA monomer is a single-stranded DNA translocase but not a processive helicase in vitro. *J. Biol. Chem.*, **282**, 27076–27085.

26. Janscak,P., Garcia,P.L., Hamburger,F., Makuta,Y., Shiraishi,K., Imai,Y., Ikeda,H. and Bickle,T.A. (2003) Characterization and mutational analysis of the RecQ core of the bloom syndrome protein. *J. Mol. Biol.*, **330**, 29–42.

27. Yang,Y., Dou,S.X., Xu,Y.N., Bazeille,N., Wang,P.Y., Rigolet,P., Xu,H.Q. and Xi,X.G. (2010) Kinetic mechanism of DNA unwinding by the BLM helicase core and molecular basis for its low processivity. *Biochemistry*, **49**, 656–668.

28. Velankar,S.S., Soultanas,P., Dillingham,M.S., Subramanya,H.S. and Wigley,D.B. (1999) Crystal structures of complexes of PcrA DNA helicase with a DNA substrate indicate an inchworm mechanism. *Cell*, **97**, 75–84.

29. Levin,M.K., Gurjar,M. and Patel,S.S. (2005) A Brownian motor mechanism of translocation and strand separation by hepatitis C virus helicase. *Nat. Struct. Mol. Biol.*, **12**, 429–435.

30. Tomko,E.J., Fischer,C.J., Niedziela-Majka,A. and Lohman,T.M. (2007) A nonuniform stepping mechanism for E. coli UvrD monomer translocation along single-stranded DNA. *Mol. Cell*, **26**, 335–347.

31. Lucius,A.L. and Lohman,T.M. (2004) Effects of temperature and ATP on the kinetic mechanism and kinetic step-size for E. coli RecBCD helicase-catalyzed DNA unwinding. *J. Mol. Biol.*, **339**, 751–771.

32. Dumont,S., Cheng,W., Serebrov,V., Beran,R.K., Tinoco,I. Jr, Pyle,A.M. and Bustamante,C. (2006) RNA translocation and unwinding mechanism of HCV NS3 helicase and its coordination by ATP. *Nature*, **439**, 105–108.

33. Henn,A., Cao,W., Hackney,D.D. and De La Cruz,E.M. (2008) The ATPase cycle mechanism of the DEAD-box rRNA helicase, DbpA. *J. Mol. Biol.*, **377**, 193–205.

34. Brune,M., Hunter,J.L., Corrie,J.E. and Webb,M.R. (1994) Direct, real-time measurement of rapid inorganic phosphate release using a novel fluorescent probe and its application to actomyosin subfragment 1 ATPase. *Biochemistry*, **33**, 8262–8271.

35. Kuhlman,P.A. and Bagshaw,C.R. (1998) ATPase kinetics of the Dictyostelium discoideum myosin II motor domain. *J. Muscle. Res. Cell Motil.*, **19**, 491–504.

36. Ritchie,M.D., Geeves,M.A., Woodward,S.K. and Manstein,D.J. (1993) Kinetic characterization of a cytoplasmic myosin motor domain expressed in Dictyostelium discoideum. *Proc. Natl Acad. Sci. USA*, **90**, 8619–8623.

37. Woodward,S.K., Geeves,M.A. and Manstein,D.J. (1995) Kinetic characterization of the catalytic domain of Dictyostelium discoideum myosin. *Biochemistry*, **34**, 16056–16064.

38. Toseland,C.P., Martinez-Senac,M.M., Slatter,A.F. and Webb,M.R. (2009) The ATPase cycle of PcrA helicase and its coupling to translocation on DNA. *J. Mol. Biol.*, **392**, 1020–1032.

39. Brendza,K.M., Cheng,W., Fischer,C.J., Chesnik,M.A., Niedziela-Majka,A. and Lohman,T.M. (2005) Autoinhibition of Escherichia coli Rep monomer helicase activity by its 2B subdomain. *Proc. Natl Acad. Sci. USA*, **102**, 10076–10081.

40. Gyimesi,M., Sarlós,K., Derényi,I. and Kovács,M. (2010) Streamlined determination of processive run length and mechanochemical coupling of nucleic acid motor activities. *Nucleic Acids Res.*, [31 January 2010, date last accessed].

41. Zhang,X.D., Dou,S.X., Xie,P., Hu,J.S., Wang,P.Y. and Xi,X.G. (2006) Escherichia coli RecQ is a rapid, efficient, and monomeric helicase. *J. Biol. Chem.*, **281**, 12655–12663.

42. Dillingham,M.S., Wigley,D.B. and Webb,M.R. (2000) Demonstration of unidirectional single-stranded DNA translocation by PcrA helicase: measurement of step size and translocation speed. *Biochemistry*, **39**, 205–212.

43. Fischer,C., Fitzgerald,D. and Yamada,K. (2009) Kinetic Mechanism for Single stranded DNA binding and Translocation by S. cerevisiae Isw2. *Biochemistry*, **48**, 2960–2968.

44. Martinez-Senac,M.M. and Webb,M.R. (2005) Mechanism of translocation and kinetics of DNA unwinding by the helicase RecG. *Biochemistry*, **44**, 16967–16976.

45. Korolev,S., Hsieh,J., Gauss,G.H., Lohman,T.M. and Waksman,G. (1997) Major domain swiveling revealed by the crystal structures of complexes of E. coli Rep helicase bound to single-stranded DNA and ADP. *Cell*, **90**, 635–647.

46. Buttner,K., Nehring,S. and Hopfner,K.P. (2007) Structural basis for DNA duplex separation by a superfamily-2 helicase. *Nat. Struct. Mol. Biol.*, **14**, 647–652.

47. Kim,J.L., Morgenstern,K.A., Griffith,J.P., Dwyer,M.D., Thomson,J.A., Murcko,M.A., Lin,C. and Caron,P.R. (1998) Hepatitis C virus NS3 RNA helicase domain with a bound oligonucleotide: the crystal structure provides insights into the mode of unwinding. *Structure*, **6**, 89–100.

48. Andersen,C.B., Ballut,L., Johansen,J.S., Chamieh,H., Nielsen,K.H., Oliveira,C.L., Pedersen,J.S., Seraphin,B., Le Hir,H.

and Andersen,G.R. (2006) Structure of the exon junction core complex with a trapped DEAD-box ATPase bound to RNA. *Science*, **313**, 1968–1972.

49. Bono,F., Ebert,J., Lorentzen,E. and Conti,E. (2006) The crystal structure of the exon junction complex reveals how it maintains a stable grip on mRNA. *Cell*, **126**, 713–725.

50. Sengoku,T., Nureki,O., Nakamura,A., Kobayashi,S. and Yokoyama,S. (2006) Structural basis for RNA unwinding by the DEAD-box protein Drosophila Vasa. *Cell*, **125**, 287–300.

51. Gu,M. and Rice,C.M. (2010) Three conformational snapshots of the hepatitis C virus NS3 helicase reveal a ratchet translocation mechanism. *Proc. Natl Acad. Sci. USA*, **107**, 521–528.

52. Saikrishnan,K., Powell,B., Cook,N.J., Webb,M.R. and Wigley,D.B. (2009) Mechanistic basis of 5′-3′ translocation in SF1B helicases. *Cell*, **137**, 849–859.

53. Wang,Q., Arnold,J.J., Uchida,A., Raney,K.D. and Cameron,C.E. (2009) Phosphate release contributes to the rate-limiting step for unwinding by an RNA helicase. *Nucleic Acids Res.*, **37**, 7151–7162.

54. Aregger,R. and Klostermeier,D. (2009) The DEAD box helicase YxiN maintains a closed conformation during ATP hydrolysis. *Biochemistry*, **48**, 10679–10681.

55. Guo,R.B., Rigolet,P., Ren,H., Zhang,B., Zhang,X.D., Dou,S.X., Wang,P.Y., Amor-Gueret,M. and Xi,X.G. (2007) Structural and functional analyses of disease-causing missense mutations in Bloom syndrome protein. *Nucleic Acids Res.*, **35**, 6297–6310.

56. Bernstein,D.A., Zittel,M.C. and Keck,J.L. (2003) High-resolution structure of the E.coli RecQ helicase catalytic core. *EMBO J.*, **22**, 4910–4921.

57. Betterton,M.D. and Julicher,F. (2005) Opening of nucleic-acid double strands by helicases: active versus passive opening. *Phys. Rev. E Stat. Nonlin. Soft Matter Phys.*, **71**, 011904.

58. Johnson,D.S., Bai,L., Smith,B.Y., Patel,S.S. and Wang,M.D. (2007) Single-molecule studies reveal dynamics of DNA unwinding by the ring-shaped T7 helicase. *Cell*, **129**, 1299–1309.

59. Lohman,T.M. and Bjornson,K.P. (1996) Mechanisms of helicase-catalyzed DNA unwinding. *Annu. Rev. Biochem.*, **65**, 169–214.